



1 **Variability of Lidar-Derived Particle Properties Over West Africa Due to Changes in**
2 **Absorption: Towards an Understanding**

3 Igor Veselovskii¹, Qiaoyun Hu², Philippe Goloub², Thierry Podvin², Mikhael Korenskiy¹,
4 Yevgeny Derimian², Michel Legrand², Patricia Castellanos³

5 ¹*General Physics Institute, Moscow, Russia.*

6 ²*Univ. Lille, CNRS, UMR 8518 - LOA - Laboratoire d'Optique Atmospherique, Lille F-59000,*
7 *France*

8 ³*NASA Goddard Space Flight Center, Greenbelt, USA*

9

10 **Abstract**

11 Measurements performed in Western Africa (Senegal) during the SHADOW-2 field
12 campaign are analyzed to show that spectral dependence of the imaginary part of the complex
13 refractive index (CRI) of dust can be revealed by lidar-measured particle parameters. Observations
14 in April 2015 provide good opportunity for such study, because, due to high optical depth of the
15 dust, exceeding 0.5, the extinction coefficient could be derived from lidar measurements with high
16 accuracy and contribution of other aerosol types, such as biomass burning, was negligible. For
17 instance, in the second half of April 2015, AERONET observations demonstrated a temporal
18 decrease of the imaginary part of CRI at 440 nm from approximately 0.0045 to 0.0025. This
19 decrease is in line with a change in relationship between lidar ratios (the extinction-to-
20 backscattering ratio) at 355 nm and 532 nm (S_{355} and S_{532}). In the first half of April, S_{355}/S_{532} is as
21 high as 1.5 and the backscatter Angstrom exponent A_β , is as low as -0.75, while after 15 April
22 $S_{355}/S_{532}=1.0$ and A_β is close to zero. The aerosol depolarization ratio δ_{532} for the whole April
23 exceeded 30% in the height range considered, implying that no other aerosol, except dust,
24 occurred. The performed modeling confirmed that the observed S_{355}/S_{532} and A_β values match the
25 spectrally dependent imaginary part of the refractive index as can be expected for mineral dust
26 containing iron oxides. West Africa is also known for significant biomass burning aerosol
27 emissions during the dry season in the Sahel region.

28 The second phase of the SHADOW-2 campaign was focused on evaluation of lidar ratio
29 of smoke and estimates of its dependence on relative humidity (RH). For considered five smoke
30 episodes the lidar ratio increases from 44 ± 5 sr to 66 ± 7 sr at 532 nm and from 62 ± 6 sr to 80 ± 8 sr
31 at 355 nm, when RH varied from 25% to 85%. Performed numerical simulations demonstrate, that
32 observed ratio S_{355}/S_{532} , exceeding 1.0 in the smoke plumes, can indicate to increase of the
33 imaginary part of the smoke particles in UV.

34

35

36



37 **1. Introduction**

38 Atmospheric dust provides significant impacts on the Earth's climate system and this
39 impact remains highly uncertain (IPCC report, 2013). In modeling the direct aerosol effect, the
40 vertical profile of aerosol extinction is one of the basic input parameters, and when this profile is
41 derived from the elastic backscatter lidar observations, the knowledge of the extinction-to-
42 backscatter ratio (so called lidar ratio) is essential. Although the desert dust in source regions is
43 sometimes qualified as "pure dust", it is always a mixture of various elements, e.g. iron oxides,
44 clays, quartz and calcium-rich species, which proportions can vary (Sokolik and Toon, 1999;
45 Wagner et al., 2012; Di Biagio et al., 2017, 2019 and references therein). Thus, the dust optical
46 properties, and hence the lidar ratio (S) can vary, depending on relative abundance of various
47 minerals in emission sources. Imaginary part of the complex refractive index (CRI) of different
48 minerals can vary spectrally and often exhibits an increase in UV for dust, containing iron oxides.
49 Therefore, retrieval of the dust extinction profiles from elastic backscatter lidar observation should
50 account for the spectral variation of the lidar ratio.

51 The Raman and HSRL lidars are capable to provide independent profiling of aerosol
52 backscattering and extinction coefficients (Ansmann et al., 1992), and therefore are widely used
53 to measure the lidar ratios of dust from different origins (e.g. Sakai et al., 2003; Papayannis et al.,
54 2008, 2012; Xie et al., 2008; Ansmann et al., 2011; Mamouri et al., 2013; Burton et al., 2014;
55 Nisantzi et al., 2015; Giannakaki et al., 2016; Hofer et al., 2017, 2019). The African deserts are
56 the largest sources of mineral dust and numerous studies have been conducted for quantifying the
57 particle intensive parameters (parameters independent of concentration) during dust transport from
58 this source region to Europe and over the Atlantic Ocean (Mattis et al., 2002; Amiridis et al., 2005;
59 Mona et al., 2006; Papayannis et al., 2008; Preißler et al., 2013; Rittmeister et al., 2017). The dust
60 properties are, however, modified during the transport, experiencing mixing and aging processes,
61 thus characterization of dust properties near the source regions is highly important for evaluation
62 the parameters of "pure dust". The lidar ratios at 355 nm and 532 nm (S_{355} and S_{532}) were measured
63 during the SAMUM-1 and 2 experiments in Morocco and Capo Verde respectively (Esselborn et
64 al., 2009; Tesche et al., 2009, 2011; Groß et al., 2011; Ansmann et al., 2011), as well as during the
65 more recent SHADOW-2 experiment in Senegal (Veselovskii et al., 2016, 2018). The lidar ratios
66 S_{355} and S_{532} measured during SAMUM experiments didn't present significant spectral
67 dependence. For example, for SAMUM-2 campaign, the averaged values of S_{355} and S_{532} are
68 53 ± 10 sr and 54 ± 10 sr respectively (Tesche et al., 2011). During SHADOW, however, S_{355}
69 significantly exceeded S_{532} in many dust episodes, which was linked to an increase of the
70 imaginary part of CRI of dust at 355 nm (Veselovskii et al., 2016).



71 The dust backscattering coefficient (and so lidar ratio), in contrast to extinction coefficient,
72 is sensitive to the imaginary part of CRI (Perrone et al., 2004; Gasteiger et al., 2011). Thus, it is
73 expected that enhanced absorption in the UV should increase the lidar ratio. In turn, the ratio
74 S_{355}/S_{532} should characterize the spectral variation of the imaginary part of CRI. The latest version
75 of AERONET products (3.0) provides inversions of lidar related properties, including the lidar
76 ratio, from almucantar scans with ground-based sun photometers. For these products, the shortest
77 available wavelength is 440 nm. Despite Im_{440} is lower than Im_{355} , AERONET observations still
78 show an increase of absorption at 440 nm in respect to 675 nm that yields a ratio of S_{440}/S_{675} close
79 to 1.4 for Saharan dust (Shin et al., 2018). The goal of this work is to analyze the correlation of
80 variations of Im_{440} from AERONET with measured values from lidar to reveal the effect of dust
81 absorption on lidar-derived aerosol properties. We focus on height and day-to-day variations of
82 the dust intensive properties, such as S_{355} and S_{532} , depolarization ratio (δ), as well as the extinction
83 and backscatter Ångström exponents (A_α and A_β respectively) measured during several strong dust
84 episodes in April 2015 during the SHADOW-2 campaign.

85 The smoke aerosol particles, typically originated from biomass burning, can also have a
86 pronounced spectral dependence of absorption. This is generally due to presence of carbonaceous
87 particles with organic compounds, so-called brown carbon (BrC) (Sun et al., 2007; Kirchstetter, et
88 al., 2004). The Sahel region is known for seasonal biomass burning caused by human activity on
89 combustion of agricultural waste that can produce an abundant amount of BrC. The smoke can
90 also be mixed with mineral dust during long-range transport or in the emission origin (Haywood
91 et al., 2008). During the SHADOW-2 the observation period included the biomass burning season,
92 thus an additional effort was dedicated to examination of spectral lidar ratio variability of
93 transported biomass burning aerosol under different environmental conditions and presents a
94 supplementary subject of the current study.

95 The paper is organized as follows. Section 2 describes the lidar system and provides the
96 main expressions used for the data analysis. Several strong dust episodes, in April 2015, are
97 analyzed in Section 3. In Section 4, the smoke episodes occurring from December 2015 to January
98 2016, are used to evaluate the variation of the smoke lidar ratio with relative humidity. The paper
99 is finalized with conclusion.

100

101 **2. Experimental setup and data analysis**

102 The observations were performed with LILAS multiwavelength Raman lidar during
103 SHADOW-2 campaign at Mbour, Senegal. Information related to the SHADOW-2 and
104 observation site is presented in Veselovskii et al. (2016). The LILAS is based on a tripled Nd:YAG
105 laser with a 20 Hz repetition rate and pulse energy of 90/100/100 mJ at 355/532/1064 nm. The



106 aperture of the receiving telescope is 400 mm. During the campaign, LILAS configuration
107 $(3\beta+2\alpha+1\delta)$ allowed the measurement of three particle backscattering (β_{355} , β_{532} , β_{1064}), two
108 extinction coefficients (α_{355} , α_{532}) and depolarization ratio at 532 nm (δ_{532}). To improve the
109 performance of the system at 532 nm the rotational Raman channel was used instead of the
110 vibrational one (Veselovskii et al, 2015). The measurements were performed at a 47 degrees angle
111 to horizon. The backscattering coefficients and depolarization ratios were calculated with a 7.5 m
112 range resolution (corresponding to 5.5 m vertical resolution), while range resolution of extinction
113 coefficient varied from 50 m (at 1000 m) to 125 m (at 7000 m). Particle extinction and
114 backscattering coefficients at 355 nm and 532 nm are calculated from elastic and Raman
115 backscatter signals, as described in Ansmann et al. (1992). An additional Raman reception channel
116 at 408 nm was setup for profiling the water vapor mixing ratio (WVMR) (Whiteman et al., 1992).

117 The particle depolarization ratio δ , determined as a ratio of cross- and co-polarized
118 components of the particle backscattering coefficient, was calculated and calibrated the same way
119 as described in Freudenthaler et al. (2009). To further the analysis of complex aerosol mixtures,
120 containing dust (d) and smoke (s), we can write $\beta = \beta^d + \beta^s$ and $\alpha = \alpha^d + \alpha^s$. The depolarization
121 ratio of such a mixture is therefore:

$$122 \quad \delta = \frac{\left(\frac{\delta^d}{1+\delta^d}\right)\beta^d + \left(\frac{\delta^s}{1+\delta^s}\right)\beta^s}{\frac{\beta^d}{1+\delta^d} + \frac{\beta^s}{1+\delta^s}} \quad (1)$$

123 Here δ^d and δ^s are the particle depolarization ratios of dust and smoke components respectively.

124 To characterize the spectral dependence of the extinction (α) and backscattering (β)
125 coefficients, corresponding Ångström exponents are introduced as:

$$126 \quad A_\alpha = \frac{\ln\left(\frac{\alpha_{\lambda_1}}{\alpha_{\lambda_2}}\right)}{\ln\left(\frac{\lambda_2}{\lambda_1}\right)} \quad \text{and} \quad A_\beta = \frac{\ln\left(\frac{\beta_{\lambda_1}}{\beta_{\lambda_2}}\right)}{\ln\left(\frac{\lambda_2}{\lambda_1}\right)} \quad (2)$$

127 Where α_{λ_1} , α_{λ_2} , β_{λ_1} , β_{λ_2} are the extinction and backscattering coefficients at wavelengths λ_1 and
128 λ_2 . For the mixture of smoke and dust, the extinction Ångström exponent (EAE) can be calculated

129 from the ratio $\frac{\alpha_{\lambda_1}}{\alpha_{\lambda_2}}$:



$$130 \quad \frac{\alpha_{\lambda_1}}{\alpha_{\lambda_2}} = \frac{\alpha_{\lambda_1}^d + \alpha_{\lambda_1}^s}{\alpha_{\lambda_2}^d + \alpha_{\lambda_2}^s} = \frac{\alpha_{\lambda_1}^d \left(1 + \frac{\alpha_{\lambda_1}^s}{\alpha_{\lambda_1}^d}\right)}{\alpha_{\lambda_2}^d \left(1 + \frac{\alpha_{\lambda_2}^s}{\alpha_{\lambda_2}^d}\right)} = \frac{\alpha_{\lambda_1}^d \left(1 + \frac{\alpha_{\lambda_2}^s \left(\frac{\lambda_2}{\lambda_1}\right)^{A_\alpha^s}}{\alpha_{\lambda_2}^d \left(\frac{\lambda_2}{\lambda_1}\right)^{A_\alpha^d}}\right)}{\alpha_{\lambda_2}^d \left(1 + \frac{\alpha_{\lambda_2}^s}{\alpha_{\lambda_2}^d}\right)} = \frac{\alpha_{\lambda_1}^d \left(1 + \frac{\alpha_{\lambda_2}^s}{\alpha_{\lambda_2}^d} \left(\frac{\lambda_2}{\lambda_1}\right)^{(A_\alpha^s - A_\alpha^d)}\right)}{\alpha_{\lambda_2}^d \left(1 + \frac{\alpha_{\lambda_2}^s}{\alpha_{\lambda_2}^d}\right)} \quad (3)$$

131 Here A_α^d and A_α^s are the extinction Ångström exponents of dust and smoke. The Ångström
 132 exponent of the mixture is obtained from (3):

$$133 \quad A_\alpha = \frac{\ln \frac{\alpha_{\lambda_1}}{\alpha_{\lambda_2}}}{\ln \frac{\lambda_2}{\lambda_1}} = A_\alpha^d + \frac{1}{\ln \frac{\lambda_2}{\lambda_1}} \ln \left[\frac{\left(1 + \frac{\alpha_{\lambda_2}^s}{\alpha_{\lambda_2}^d} \left(\frac{\lambda_2}{\lambda_1}\right)^{(A_\alpha^s - A_\alpha^d)}\right)}{\left(1 + \frac{\alpha_{\lambda_2}^s}{\alpha_{\lambda_2}^d}\right)} \right] \quad (4)$$

134 The backscattering Ångström exponent (BAE) can be calculated in a similar way. And finally, the
 135 lidar ratio of the aerosol mixture is calculated as:

$$136 \quad S = \frac{S^d \beta^d + S^s \beta^s}{\beta^d + \beta^s} = S^d + \frac{\beta^s}{\beta} (S^s - S^d) \quad (5)$$

137 where S^d and S^s are the lidar ratios of dust and smoke.

138

139 3. Dust observations in March and April 2015

140 The aerosol over West Africa presents strong seasonal variations. The spring is
 141 characterized by strong dust emission, while, during winter season, intense forest fires occurring
 142 in the equatorial regions emit smoke particles that are transported over Senegal. The SHADOW-
 143 2 campaign included the following periods of measurements: 13 March – 25 April 2015, 8–25
 144 December 2015 and 5–24 January 2016, so numerous dust and smoke episodes were observed. In
 145 our analysis of lidar-derived aerosol properties, we considered also aerosol columnar properties
 146 provided by AERONET (Holben et al. 1998) and aerosol profiles predicted by the Modern-Era
 147 Retrospective analysis for Research and Applications, Version 2 (MERRA-2) aerosol reanalysis
 148 (Gelaro et al., 2017; Randles et al., 2017). MERRA-2 is the first long-term global reanalysis to
 149 assimilate space-based aerosol observations and include their radiative coupling with atmospheric
 150 dynamics. MERRA-2 is driven by the Goddard Earth Observing System (GEOS) model version 5
 151 that includes the Goddard Chemistry, Aerosol, Radiation and Transport (GOCART) module.
 152 GOCART models the sources, sinks, and transformation of the following five aerosol species as
 153 external mixtures: dust, organic carbon (OC), black carbon (BC), sulfates (SU) and sea salt (SS).
 154 Dust and sea salt are represented by five non-interacting size bins, and have wind-speed dependent



155 emissions. The MERRA-2 reanalysis assimilates AOD observations from the twin Moderate
156 Resolution Imaging Spectroradiometer (MODIS) instruments, MODIS-Terra and MODIS-Aqua,
157 as well as the AERONET ground-based sun photometer network. In addition, the profiles of
158 meteorological variables (P, T, RH), provided by radio-sondes at the Dakar airport, located ~70
159 km from the M'bour site, were also available. The relative humidity (RH) profiles over the M'bour
160 site were calculated from the combination of lidar-derived WVMR and temperature profile from
161 radiosounding.

162 Fig.1 shows the aerosol optical depth at 532 nm (AOD_{532}) for March, April and December
163 2015 recalculated from AERONET AOD at 500 nm using 440-675 nm Ångström exponent. The
164 same figure shows the AODs for the five aerosol species used in MERRA-2 model, such as dust,
165 organic carbon (OC), black carbon (BC), sulfates (SU) and sea salt (SS). The optical depths
166 provided by MERRA-2 and AERONET are in a good agreement. Dust is the predominant aerosol
167 component for all three months with the highest values of AOD in April. The contribution of
168 organic carbon (the main component of the biomass burning products) is significant in December,
169 when the forest fire season starts in equatorial regions, though noticeable amount of OC is
170 predicted also for March and for the beginning of April. The contribution of BC and SU to the
171 total AOD is low: the sum of the corresponding AODs is below 0.1 for all three months.

172 The single scattering albedo (SSA) over the M'Bour site in 2015 provided by AERONET
173 at 440 and 675 nm is shown in Fig.2. The SSA_{675} is above 0.97 for March – April period, but at
174 440 nm dust absorption is stronger and, in March, SSA_{440} is about 0.9. However, in the middle of
175 April, SSA_{440} increases up to 0.95, indicating that aerosol becomes less absorbing at shorter
176 wavelengths. We can thus expect that variation of SSA at 355 nm between April and March should
177 be even stronger. In our study we consider two groups of observation. The first group corresponds
178 to the beginning of April, when SSA at 440 nm was lower. The second group covers the second
179 half of April, when SSA at 440 nm increased. By analyzing these two groups we expect to reveal
180 the effect of aerosol absorption, on lidar-derived aerosol properties.

181

182 **3.1. Dust episode on 1 – 4 April 2015**

183 In the beginning of April the dust was transported by Continental trades (Harmattan) from
184 the northeastern/eastern drylands. For period 1 - 4 April, as follows from Fig.1b, the AOD_{532} over
185 Dakar increased up to 1.0. Fig.3 shows spatio-temporal distributions of the aerosol backscattering
186 coefficient β_{532} , particle depolarization ratio δ_{532} , and water vapor mixing ratio for the nights 1-2,
187 2-3 and 3-4 April 2015. Corresponding back-trajectories, shown in Fig.4, demonstrate that, on 1-
188 2 and 2-3 April, air masses at all heights arrive from the North-East, whereas on 3-4 April the air
189 masses above 2500 m are advected from the East. These air masses are characterized by higher



190 humidity and may contain biomass-burning products. During these three nights, depolarization
191 ratio and WVMR present some evolution. On 1-2 April δ_{532} exceeds 30% and does not change
192 significantly within the dust layer, even if some decrease is observed above 2000 m after 03:00
193 UTC. By 3-4 April the depolarization ratio above 2500 m decreases below 25%, simultaneously
194 with increase of the WVMR. During the dust episode, the relative humidity did not exceed 20%
195 on 1-3 April, but on 3-4 April it increased up to 40% above 2500 m.

196 Vertical profiles of dust particle properties such as aerosol extinction coefficients α_{355} , α_{532} ,
197 particle depolarization ratio δ_{532} and lidar ratios S_{355} , S_{532} are shown on Fig.5 for the three
198 observation periods on 1, 2-3 and 3-4 April 2015. The corresponding extinction and backscatter
199 Ångström exponents, calculated for 355 and 532 nm wavelengths, are presented in Fig.6. During
200 all three observation periods A_α is slightly negative ($A_\alpha = -0.1 \pm 0.1$) up to 2000 m. For the dust
201 component, MERRA-2 provides value of $A_\alpha = -0.14$, which agrees with observations. Above 2000
202 m, A_α exhibits some increase, which is most significant on 3-4 April, when A_α reaches 0.3 ± 0.1 at
203 4000 m height. Simultaneous decrease of δ_{532} indicates to the possible presence of smoke particles
204 above 2000 m. The backscatter Ångström exponent A_β , in contrast with A_α , is sensitive to the
205 spectral dependence of the imaginary part of CRI, thus yielding complicated vertical variability of
206 A_β . In particular, on 2-3 April A_β decreases from -0.5 to -0.7 within 1500–2500 m height range,
207 when A_α remains stable.

208 As follows from Fig.5, on 1 April the lidar ratio $S_{355} = 70 \pm 6$ sr does not change with height,
209 while S_{532} gradually decreases from 60 ± 5 sr at 1000 m to 50 ± 4 sr at 3000 m height. On sessions
210 that followed (Fig.5b,c) the lidar ratios at both 355 nm and 532 nm decreased. Thus, the range of
211 lidar ratios variation for the dust episode on 1-4 April is 60-70 sr at 355 nm and 45-60 sr at 532
212 nm. The lidar ratios (S_{355} and S_{532}) modeled by MERRA-2 for the dust component are also shown
213 on Fig. 5. Corresponding values are of 70 sr and 42 sr respectively and do not vary with altitude
214 as the model optical properties of all dust size bins based on spectral complex refractive indices
215 from the Optical Properties of Aerosols and Clouds (OPAC) tables (Hess et al. 1998) and the
216 spheroidal shape models developed by Meng et al. (2010) are the same and fixed, as dust is treated
217 as homophobic. Modeled value S_{355} is near the top of the range of observed values, while modeled
218 S_{532} underestimates the observations.

219 The gradual decrease of S_{532} with height in Fig.5a,c is however unusual. There are, at least,
220 two possible reasons to explain S_{532} height variation. The first one can be the presence of non-dust
221 particles, for example, smoke. The second reason is that the properties (composition) of dust
222 change with height. If non-dust particles are present, the particle intensive properties, such as S , δ
223 and A_α should vary with height in consistent way. The MERRA-2 modeling reported in Fig.1



224 shows that in the beginning of April the organic carbon is the second main contributor to the AOD,
225 after dust. We should recall, however, that the model can provide a realistic range of OC variation,
226 however not necessarily reproducing the exact spatio-temporal distribution of OC extinction
227 coefficient.

228 In the dust episode considered, the most significant smoke contribution was observed on
229 3-4 April. Fig.7a shows the profiles of measured α_{355} and α_{532} together with MERRA-2 modeled
230 extinction coefficients at 532 nm for five aerosol components. The extinction Ångström exponents
231 measured by lidar and modeled by MERRA-2 for dust component are given by Fig.7b. The same
232 figure shows also the lidar derived water vapor mixing ratio profile together with the relative
233 humidity. At low altitudes (below 2500 m), where aerosol is represented by pure dust, the
234 measured and modeled values of extinction coefficients are close. Above 2500 m the measured
235 value of α_{355} exceeds that of α_{532} , indicating the presence of smoke particles, while modeled
236 contribution of OC to the total extinction is very low. The measured extinction Ångström exponent
237 is about -0.1 below 2000 m, which well agrees with modeling results for pure dust. Increase of
238 WVMR and RH above 2000 m coincides with growth of the A_α . For the considered case, the
239 model reproduces correctly the dust loading, but underestimates the smoke contribution. At 3500
240 m, the difference between measured and modeled α_{532} is about 0.045 km^{-1} which can be attributed
241 to the smoke contribution.

242 Dust and smoke particles contributions to the total backscattering coefficient can be also
243 separated on the basis of the depolarization measurements, assuming that depolarization ratios of
244 these particles are known (Tesche et al., 2009). The results of such decomposition are presented
245 in Fig.7c, assuming 35% and 7% for dust and smoke depolarization ratio, respectively. The
246 contribution of smoke to the total β_{532} at 3500 m is $0.0009 \text{ km}^{-1}\text{sr}^{-1}$. For the smoke lidar ratio of 50
247 sr at 532 nm (validity of this choice will be discussed in section 3.3), the smoke extinction
248 coefficient is about 0.045 km^{-1} . This value agrees well with smoke contribution obtained from
249 Fig.7a at 3500 m and thus can be used for estimating the smoke effect on the intensive aerosols
250 properties derived from lidar measurements.

251 The depolarization ratio of the “dust-smoke” mixture, calculated with expression (1),
252 matches the observed value since decomposition in Fig.7c is based on depolarization
253 measurements. The Ångström exponent at 3500 m computed with (4) for $\alpha_{532}^s = 0.045 \text{ km}^{-1}$, α_{532}^d
254 $= 0.147 \text{ km}^{-1}$, $A_\alpha^d = -0.1$ and $A_\alpha^s = 1.0$ yields $A_\alpha = 0.2$, which matches observed value 0.25 ± 0.1 .
255 Hence, the observed variation of A_α above 2000 m on 3-4 April is explained by smoke
256 contribution. In a similar way, using (5) we can estimate the smoke lidar ratio (S_{532}^s) that would



257 match the observed decrease of S_{532} . To explain decrease of the lidar ratio at 3500 m from 50 sr
258 to 45 sr, the smoke lidar ratio should be about 25 sr, which is unrealistically small. Such small
259 lidar ratio could be attributed to the maritime aerosol, but then the lidar ratios at both wavelengths
260 should decrease simultaneously. Recall that on 1-2 April smoke contribution was significantly
261 lower, while decrease of S_{532} is about 10 sr. Thus, smoke particles presence cannot explain the
262 observed decrease of S_{532} and it should be probably attributed to changes of dust composition (and
263 so the imaginary part) with height.

264 Smoke lidar ratio is usually assumed to be higher than that of dust (Burton et al., 2014),
265 meanwhile in Fig 5c the lidar ratio S_{532} is not increased in presence of the smoke particles. It should
266 however be noticed that our results were obtained at low RH. The smoke particles are hygroscopic
267 and the lidar ratio should increase with RH. The way to characterize S_{532}^s over Dakar site can be
268 based on the analysis of the lidar measurements during smoke episodes within height range where
269 smoke contribution becomes predominant. The results of such analysis will be discussed later in
270 section 3.3.

271

272 **3.2. Dust episodes on 14 and 24 April 2015.**

273 In the second part of April 2015, dust AOD_{532} exceeded 1.0 (Fig.1b) and contributions of
274 other aerosol components were insignificant. Meanwhile, as follows from Fig.2, SSA_{440} increased
275 after 15 April, thus dust became less absorbing in UV, which should influence the lidar-derived
276 aerosol intensive properties. Fig.8 shows extinction coefficients and lidar ratios at 355 nm and 532
277 nm, together with depolarization ratio δ_{532} and the Ångström exponents A_α and A_β observed on
278 14 April (00:00 – 05:00 UTC) and 23-24 April (23:00-06:00 UTC). The first case is a “transition
279 day” when SSA_{440} starts to increase. Extinction profiles presented in Fig.8a show that two dust
280 layers can be distinguished. In the first layer (below 2.5 km), aerosol intensive properties are
281 similar to that of 1-4 April with $S_{355} > S_{532}$, slightly negative $A_\alpha = -0.1$ and A_β as low as -0.35. In
282 the second layer S_{355} and S_{532} coincide and both A_α and A_β are close to zero. The depolarization
283 ratio in the second layer is about 31%, slightly lower than in the first one. Thus, we can assume
284 that increase of the imaginary part in UV in the first layer is more significant, than in the second
285 one. From back-trajectories given in Fig.9, we can conclude that the air masses in the first layer
286 originate from the Northeastern/Eastern drylands, while in the second layer the air masses arrive
287 from the East. After 14 April, S_{355} and S_{532} coincided for the whole height range and results
288 obtained on 23-24 April (Fig.8 c, d) are the example of such observations. Back-trajectories show
289 that the air masses at both 2.0 and 3.0 km height are transported from East. The ratio S_{355}/S_{532} is



290 close to 1.0 within the whole dust layer and both Ångström exponents A_α , A_β are close to zero.
291 Thus, the results from Fig.8, 9 are indicating that lidar-derived aerosol properties depend on the
292 dust source origin.

293

294 **3.3 Analysis of lidar ratio variations in March – April 2015**

295 Fig.10 summarizes the lidar ratio measurements for period from 29 March to 24 April 2015
296 (first phase of SHADOW ended on 25 April). Here we focus on the properties of the “pure dust”,
297 thus do not show results before 29 March, when AOD was lower and the contribution of other
298 aerosol types could be significant (Fig.1). For the Fig.10 we have chosen height intervals, where
299 S value is stable and δ exceeds 30%. For example, on 14 and 24 April lidar ratios are averaged
300 inside 2.7-3.7 km and 2.0-4.0 km layers respectively. For the period considered, S_{355} and S_{532} vary
301 in the ranges 50 sr – 80 sr and 45 sr – 60 sr respectively with a mean values of 62 sr and 51 sr.
302 Enhanced variability of S_{355} compared to S_{532} can be explained by variation of the imaginary part
303 at 355 nm. At the beginning of the 29 March and 8 April dust episodes, S_{355}/S_{532} ratio is as high as
304 1.5 and then gradually decreases. After 14 April, S_{355}/S_{532} ratio becomes close to 1.0, thus S
305 presents no spectral dependence.

306 The day-to-day variation of aerosol column properties, including the spectrally dependent
307 complex refractive index, can be obtained from AERONET (Holben et al., 1998). Fig.11 shows
308 the imaginary part of the refractive index at 440 nm and 675 nm (Im_{440} , Im_{675}) provided by
309 AERONET for the same period of time as in Fig.10. The Im_{440} strongly decreases after 14 April,
310 correlating with the decrease of S_{355}/S_{532} ratio in Fig.10, which corroborates the suggestion, that
311 variations of S_{355}/S_{532} ratio are related to variation of dust absorption in UV. The retrieved real
312 part (Re) of the complex refractive index oscillates around $Re=1.45$ and shows no significant
313 spectral dependence. Correlation between enhancement of Im_{440} , with in respect to Im_{675} , and
314 increase of lidar-derived S_{355}/S_{532} is clearly seen in Fig.12, showing time – series of difference
315 $Im_{440}-Im_{675}$ and S_{355}/S_{532} ratio.

316 To analyze the variations of observed lidar ratios and the Ångström exponents, a simplified
317 numerical simulation has been performed. For a realistic modeling of the dust lidar ratio, various
318 mixtures of different mineral components and particles shapes should be considered. Sensitivity
319 of the modeling results to the dust mixture parameters was demonstrated in study of Gasteiger et
320 al. (2011). Such detailed modeling, however, is out of the scope of the present paper. Here we only
321 intend to evaluate the main impact when the imaginary part of CRI is modified.

322 The lidar ratio depends not only on the complex refractive index but also on the dust
323 particle size distribution (PSD). The PSDs provided by AERONET on 2 and 23 April 2015 (three



324 distributions for each day) are shown in Fig.13. The PSDs are similar and the effective radii for
325 both days are about $0.75 \mu\text{m}$, thus, difference in S observed for 2 and 23 April should be related
326 mainly to the complex refractive index. Fig.14a presents modeled S_{355} and S_{532} lidar ratios together
327 with the extinction and backscattering Ångström exponents A_α , A_β as a function of the imaginary
328 part. Computations were performed for the AERONET derived size distribution on 23 April from
329 Fig.13 using the assembly of randomly oriented spheroids (Dubovik et al., 2006) with the real part
330 $\text{Re}=1.55$. S_{355} and S_{532} increase with the imaginary part and the ratio S_{355}/S_{532} is about 1.1.
331 Extinction coefficient is slightly sensitive to the imaginary part, thus increase of S in Fig.14 is due
332 to decrease of backscattering coefficient with Im . The modeled A_α is about $A_\alpha=0.1$, while A_β
333 decreases with Im to $A_\beta=-0.2$. To estimate the influence of a spectrally dependent imaginary part
334 $\text{Im}(\lambda)$ on A_β , we have also performed computations assuming a fixed $\text{Im}_{532}=0.002$ and only Im_{355}
335 is free to vary. Corresponding results are shown in Fig.14a with open stars. Spectral dependence
336 of the imaginary part significantly decreases A_β : for $\text{Im}_{355}=0.005$ ($\text{Im}_{355} - \text{Im}_{532}=0.003$), A_β
337 decreases to -0.75 .

338 We should recall however, that for the second half of April the observed ratio S_{355}/S_{532} ,
339 was about 1.0, and both extinction and backscatter Ångström exponents were close to zero. To
340 figure out the kind of PSD that would reproduce those observations, we retrieved the PSD from
341 $3\beta+2\alpha$ measurements, as described in Veselovskii et al. (2002, 2010). For that purpose, data from
342 23-24 April (Fig.8), averaged within 2-3 km layer, were inverted and corresponding PSD is shown
343 in Fig.13 with red line. Inversion was performed for the assembly of randomly oriented spheroids,
344 in assumption of spectrally independent refractive index. Due to the limited number of input data
345 (five) we are able to reproduce only the main features of the PSD. The maximum of this lidar
346 derived PSD is shifted towards larger radii, with respect to the AERONET size distribution, but at
347 the same time, retrieved PSD contains significant contribution from the fine particles. The
348 simulation results for this lidar derived PSD, are given by Fig.14b. The lidar ratios S_{355} , S_{532} for
349 all values of the imaginary part are close. The backscatter and extinction Ångström exponents are
350 close to zero, matching the observations of the second half of April 2015. Thus simulation results
351 demonstrate dependence on the PSD chosen, but in both cases these lead to the same conclusion:
352 observed low values of A_β can not be reproduced without accounting for spectral dependence of
353 the imaginary part.

354 To compare computations and observations, information upon Im_{355} and Im_{532} values is
355 needed. The recently measured refractive indices of dust, sampled at different regions of Africa,
356 are presented by Di Biagio et al. (2019). In particular, for the countries located North and East of
357 Senegal, the imaginary parts at 370, 470, 520, 660 nm are of 0.0043, 0.0033, 0.0026, 0.0013 for



358 Mauritania and 0.0048, 0.0038, 0.0030, 0.0024 for Mali respectively. The highest values of lidar
359 ratios, observed in our measurements, are about 60 sr and 80 sr at 532 nm and 355 nm respectively.
360 Corresponding imaginary parts of CRI from Fig.14 can be estimated as $Im_{532}=0.002-0.003$ and
361 $Im_{355}=0.005-0.006$, which agrees with results presented by Di Biagio et al. (2019). Assuming
362 $Im_{355}=0.005$ and $Im_{532}=0.002$, the modeled ratio S_{355}/S_{532} is about 1.44 and A_{β} is about -0.75 for
363 both AERONET and lidar derived PSDs, which again reasonably agrees with observations. The
364 modeling performed is very simplified, still it confirms that observed values of S_{355}/S_{532} ratio and
365 A_{β} can be explained by the spectral dependence of the imaginary part of CRI.

366 Thus, based on our measurement results, two types of dust can be distinguished. The first
367 type has high S_{355}/S_{532} ratio (up to 1.5). Such kind of dust is characterized by increase of the
368 imaginary part in UV and it was observed, for example, during 29 March and 10 April episodes.
369 For the second type, the ratio $S_{355}/S_{532}\approx 1.0$, so variation of the imaginary between 532 and 355 nm
370 wavelengths should be smaller than for the first type. Such dust was observed in the second half
371 of April 2015. Both types are characterized by high depolarization ratio, δ_{532} , exceeding 30%, so
372 depolarization measurements at 532 nm are not capable to discriminate between these two types
373 of dust.

374 Difference in the observed dust properties is probably related to the mineralogical
375 characteristics in the source region. From the back-trajectories analysis presented in Figs. 4 and 9
376 one can suppose that the first type of dust was transported from the North–East, while the second
377 type from the East. In order to verify if a difference in the dust emission source region and transport
378 take place, we also analyzed the Infrared Difference Dust Index (IDDI) derived from the Meteosat
379 Second Generation (MSG) geostationary satellite imagery in thermal infrared (TIR). The IDDI is
380 developed by Legrand et al. (1985, 2001) originally for the Meteosat First Generation (MFG) and
381 is based on impact of airborne mineral dust on TIR radiation emitted by terrestrial surface. The
382 physical principle of the IDDI derivation is in thermal contrast between terrestrial surface and
383 atmosphere and the best sensitivity is found at around noon time when the surface temperature is
384 maximal (Legrand et al., 1988). The IDDI product shows that brightness temperature of terrestrial
385 surface observed by satellite can be reduced up to about 50°K in presence of airborne mineral dust,
386 while reduction by about 10°K already indicates a major dust event (Legrand et al., 2001). A direct
387 relationship between the IDDI and aerosol optical thickness in solar spectrum and visibility was
388 also found (Legrand et al., 2001). It should be mentioned here that the IDDI was initially developed
389 for MFG and the absolute consistence with the IDDI values from MSG should be examined due
390 to differences in spatial and spectral resolutions between two sensors. However, the physical
391 principles used for the IDDI determination are the same and a direct application of the MFG IDDI
392 algorithm to MSG was found as possible. Moreover, tests showed that the absolute values of IDDI



393 for a coincident overlapping period of MFG and MSG are very close. Nevertheless, employment
394 of the IDDI from MSG is indeed applicable for the required in the current analysis purpose of
395 solely dust spatial patterns detection.

396 The IDDI calculations, applied to the MSG images taken during the field campaign, clearly
397 show a major dust event in northern and central Africa. The elevated IDDI values over Senegal
398 are also visible. The IDDI images show distinguishable changes in the emission sources and
399 transport features during the different phases of the observations. For instance, Fig. 15 shows that
400 the dust emissions during the first phase of the event are originated in south Algeria, Mauritania
401 and Mali (examples of images from 29 and 30 March 2015). Weeks later, spatial patterns of the
402 elevated IDDI are shifted to south and show source regions in south of Niger (Fig.15c, d). Of
403 course, attribution of emission sources mineralogy to aerosol spectral absorption is a complex task
404 (Alfaro., et al 2004; Lafon et al., 2006; Di Biagio et al., 2017, 2019) and it is difficult to point to a
405 specific source that could clearly explain the observed in this study change in the aerosol absorbing
406 properties. However, the IDDI images clearly suggest a change in the dust transport regime that is
407 consistent with the change in the dust optical properties.

408

409 **4. Smoke episodes in December 2015 – January 2016**

410 During the SHADOW campaign, we had several strong smoke episodes in December 2015
411 – January 2016, when air mass transported the products of biomass burning from the areas of
412 intensive forest fires in equatorial region. The relative humidity in the advected smoke layers
413 varied from episode to episode, allowing evaluation of the RH influence on the smoke lidar ratios
414 S_{355} , S_{532} . The spatio-temporal evolution of the particle backscattering coefficient and
415 depolarization ratio at 532 nm, during the 14-15 December 2015 smoke episode, is given in Fig.16.
416 The same figure shows also the water vapor mixing ratio, a convenient tracer to identify wet air
417 mass arrived from the equatorial region. The smoke particles are usually contained in elevated
418 layers, being mixed with dust (Veselovskii et al., 2018). The height ranges where the smoke
419 particles are predominant can be identified by low depolarization ratio and enhanced WVMR. For
420 event considered, the smoke particles are predominant above 1500 m after midnight.

421 The vertical profiles of α_{355} , α_{532} , S_{355} , S_{532} , A_α , A_β together with the water vapor mixing
422 ratio and the relative humidity, for 15 December (04:00 – 06:00 UTC), are shown in Fig.17. The
423 same figure presents decomposition of β_{532} to the dust and smoke contributions, based on
424 depolarization measurements (Tesche et al., 2011). The smoke episodes are characterized by
425 different relative humidity within the elevated layer. On 15 December, RH is about 40% in the
426 1500 – 2100 m range and the ratio $\frac{\beta_{532}^s}{\beta_{532}}$ is about of 0.57 at 2000 m. The lidar ratio S_{532} decreases



427 from 50 sr to 44 sr in 1000 m - 2000 m range, while S_{355} rises from 58 sr to 67 sr, thus S_{355}
428 significantly exceeds S_{532} . We should recall that lidar ratios presented in Fig.17 are attributed to
429 dust- smoke mixture. In principle, we can estimate S_{532}^s using Eq.5, because the ratio $\frac{\beta_{532}^s}{\beta_{532}}$ is
430 available. Corresponding S_{532}^s profile obtained for assumed $S_{532}^d = 50$ sr is shown in Fig.17a (black
431 line). S_{532}^s is about 40 sr at 2000 m and it is close to measured S_{532} value. In the smoke layer, the
432 extinction Ångström exponent A_α , can exceed A_β , due to negative contribution of A_β^d . In
433 particular, on 15 December A_α is about 1.1, while A_β is close to zero.

434 To estimate the dependence of smoke lidar ratios S_{355} and S_{532} on RH, five smoke episodes
435 on 14-15, 15-16, 22-23, 24-25 December 2015 and 19-20 January 2016 were analyzed. S_{532} and
436 S_{355} , together with relative humidity and the $\frac{\beta_{532}^s}{\beta_{532}}$ ratio are summarized, for these episodes, in
437 Table 1. The heights chosen correspond to the values of relative humidity close to maximum. The
438 calculated values of RH are characterized by high uncertainties, because lidar and sonde
439 measurements are not collocated. Estimations of corresponding uncertainties are also given by
440 Table 1. The lidar ratio values from Table 1 are plotted in Fig.18 as a function of RH. These plots,
441 however, should be taken with care, because, for different days the smoke particles could have
442 different chemical composition, thus results may depend not only on RH. Moreover, the dust
443 particles occurring in the elevated layers, as discussed, can introduce an additional ambiguity in
444 the results. On 15 December (04:00 – 06:00 UTC) the lidar ratio $S_{532} = 44 \pm 5$ sr is quite low and
445 “drops out” of other sessions. Nevertheless, Fig.18 demonstrates a clear increasing trend of S with
446 RH, at both wavelengths. From this figure, one can also conclude that S_{355} always exceeds S_{532}
447 and, that S_{532} for smoke can be as small as 44 ± 5 sr at low humidity. The small values of S_{532} for
448 the “fresh smoke” (about 40 sr) were reported also by (Burton et al., 2012).

449 To compare our observations with the lidar ratios used in the MERRA-2 model, we have
450 also performed the simulation of $S_{532}^{OC}(RH)$ and $S_{355}^{OC}(RH)$ dependence for organic carbon (OC)
451 based on the particle parameters and hygroscopic growth factor from MERRA-2 model. In
452 MERRA-2 the organic carbon is the main component of the biomass burning products. The
453 imaginary part of the OC increases in UV due to the presence of “brown carbon” (BrC), which is
454 a subset of organic carbon with strong absorption in the UV region (Bergstrom et al., 2007; Torres
455 et al., 2007). The majority of BrC is emitted into the atmosphere through low-temperature,
456 incomplete combustion of biomass. In the newest development of GEOS, biomass burning OC is



457 now emitted as a new BrC tracer species that uses $Im_{532}=0.009$ and $Im_{355}=0.048$ values (Hammer
458 et al. 2016). Thus, the spectral behavior of the imaginary part of organic carbon refractive index
459 depends on contribution of the BrC fraction to the primary organic carbon and on the physical-
460 chemical processes in the smoke layer during its transportation. As a result, the spectral
461 dependence of Im can present strong variations. In our study, the computations at 355 nm were
462 performed for four values of the imaginary part of dry particles $Im_{355}=0.048, 0.03, 0.02, 0.01$. At
463 532 nm two values $Im_{532}=0.005$ and 0.009 were considered. The parameters of the dry particle size
464 distribution, the real part of CRI and the hygroscopic growth factor used in computations are given
465 in Veselovskii et al. (2018). The particles are assumed to be homogeneous spheres and an increase
466 of the volume for every RH value (calculated from the growth factor) occurs due to water uptake.
467 Thus both the real and the imaginary part of CRI depend on RH.

468 The results of the simulations, shown in Fig.18, demonstrate strong dependence of the
469 organic carbon lidar ratio on the imaginary part of dry particles and on the relative humidity. For
470 $Im_{355}=0.048$, for all RH, S_{355} is above 95 sr, which strongly exceeds the observed values. For lower
471 Im_{355} the S_{355} (RH) dependence is more pronounced and for Im_{355} within the range 0.01-0.02,
472 computed S_{355} are close to observed values. Computed S_{532} values at low RH exceed the measured
473 ones, but for $RH>70\%$ agreement between measurements and GEOS assumed optical properties
474 for OC becomes reasonable.

475 The ratio S_{355}/S_{532} for organic carbon, the same as for dust, is strongly influenced by the
476 spectral dependence of the imaginary part of CRI, hence it can be used as an indicator of Im
477 enhancement in UV. The ratios S_{355}/S_{532} , calculated from the results of modeling in Fig.18 for four
478 values of Im_{355} (0.048, 0.03, 0.02, 0.01) and $Im_{532}=0.009$, are shown in Fig.19. The ratio S_{355}/S_{532} ,
479 corresponding to $Im_{355}=0.01$, is about 1.1 in the whole range of RH. However for the imaginary
480 part of dry particles $Im_{355}=0.02$ and 0.03 the ratio S_{355}/S_{532} increases up to approximately 1.2 and
481 1.3 respectively for RH in 40%-70% range. Thus, enhanced Im_{355} of dry OC particles should
482 provide increase of S_{355}/S_{532} ratio even high RH and this is how it can be revealed. The measured
483 values of S_{355}/S_{532} are shown on the same figure. As mentioned, observation at 532 nm on 15
484 December (RH=42%) “drops out” of other sessions. For the rest of observations the ratio S_{355}/S_{532}
485 is in 1.2 – 1.3 range, and from modeling in Fig.19 the imaginary part of the dry particles at 355
486 nm is estimated to be in 0.02-0.03 range.

487

488 5. Summary and conclusion

489 Our study shows the impact of aerosol spectral absorption variation on the lidar-derived
490 aerosol properties. In contrast to extinction, the backscattering coefficient, and so the lidar ratio,
491 are sensitive to the imaginary part of CRI. Hence, S_{355}/S_{532} ratio can be an indicator of the



492 imaginary refractive index enhancement in the UV. Measurements performed during the
493 SHADOW campaign, in dust conditions, show a correlation between the decrease of Im_{440} , derived
494 from AERONET observations, and the decrease of lidar-derived S_{355}/S_{532} ratio. Namely, in the
495 second half of April 2015, S_{355}/S_{532} decreased from 1.5 to 1.0, when Im_{440} decreased from 0.0045
496 to 0.0025. Our numerical simulations confirm, that observed S_{355}/S_{532} (ratio close to 1.5) and A_{β}
497 (value close to -0.75) can be due to spectral variation of the imaginary part, attributed to iron oxides
498 contained in dust particles. Thus, April 2015 observations suggest the presence of different dust
499 types, characterized by distinct spectral dependence of $Im(\lambda)$. The analysis of backward
500 trajectories and Infrared Difference Dust Index derived from MSG geostationary satellite confirms
501 different air mass and dust particles transport features in the beginning and at the end of April.
502 Hence, the observed variations of S_{355}/S_{532} can be related to the source region mineralogy. During
503 the April, particle depolarization systematically exceeded 30%, therefore no discrimination
504 between different types of dust was possible.

505 The results presented in this study demonstrate also that, for the selected temporal interval,
506 the dust lidar ratios may present significant variation with height. Dust of different size and
507 mineralogical composition can have different deposition rate, hence, complex refractive index can
508 be height-dependent. For instance, on April 1st, the S_{532} decreased with height from 60 sr to 50 sr
509 within 1000–3000 m range, while depolarization ratio exceeded 30%. The analysis of this episode
510 showed that variation of the lidar ratio is entirely attributed to variations of dust characteristics;
511 the smoke aerosol contribution was insignificant. The data also demonstrate that a seemingly
512 uniform dust layer may have quite a complex height variation. The results therefore suggest the
513 relevance of including a varying mineralogy in radiative and climatic modeling of desert dust
514 impacts.

515 During December – January, the dry season in western Africa, our observations allowed in
516 addition the analysis of biomass burning aerosol properties. These particles are a product of the
517 seasonal forest fires and intensive agricultural waste combustion and can contain a substantial
518 amount of organic compounds, characterized by an enhanced imaginary part in UV (so called
519 BrC). For this aerosol type, the $Im(\lambda)$ dependence should increase the lidar ratio at 355 nm and
520 influence S_{355}/S_{532} . The smoke particles can be also hydrophilic and the lidar ratio can therefore
521 exhibit a strong dependence on RH. The numerical simulations performed for organic carbon,
522 which is the main component of smoke in GEOS model, demonstrated that S_{355}/S_{532} is close to 1.0
523 in the absence of spectral variation of the imaginary part; this ratio, however, can be as high as 1.8
524 for dry particles with $Im_{532}=0.009$ and $Im_{355}=0.048$. This S_{355}/S_{532} ratio decreases with RH,
525 however even for high humidity it depends on the Im_{355} value for dry particles. In particular, for
526 $Im_{355}=0.02$ and 0.03 the ratio S_{355}/S_{532} is about 1.2 and 1.3 respectively for RH in 40%-70% range.



527 Thus, observed S_{355}/S_{532} values, exceeding 1.0, could corroborate the enhancement of imaginary
528 refractive index for smoke in UV.

529 Several strong smoke episodes were observed during the SHADOW campaign. While we
530 were able to evaluate the RH profiles, the dependence of the smoke lidar ratio with RH has been
531 estimated. The results obtained should be taken as semi-qualitative only, due to possible variation
532 of smoke particles composition from episode to episode and due to the presence of dust particles.
533 Nevertheless, the results clearly demonstrate an increase of S_{532} from 44 ± 5 sr to 66 ± 7 sr and of
534 S_{355} from 62 ± 6 sr to 80 ± 8 sr, when the RH increased from 25% to 85%. The measured S_{355}/S_{532}
535 ratio varied mainly within the range 1.2 - 1.3, so comparison with modeling for OC provides the
536 estimate of Im_{355} of dry smoke particles in 0.02-0.03 range.

537 We would like to conclude that the multi-wavelengths Raman and depolarization lidar
538 measurements in western Africa enabled quite unique and comprehensive profiling of dust and
539 smoke spectral absorption properties. The results demonstrated a high variability of the lidar ratio
540 and the presence of its spectral dependence. Our study is one of the first attempts to track aerosol
541 composition variability using lidar measurements and to understand the mechanism underlying the
542 observed variations.

543

544 **Acknowledgments:** The authors are very grateful to the CaPPA project (Chemical and Physical
545 Properties of the Atmosphere), funded by the French National Research Agency (ANR) through
546 the PIA (Programme d'Investissement d'Avenir) under contract "ANR-11-LABX-0005-01" and
547 by the Regional Council "Nord-Pas de Calais" and the "European Funds for Regional Economic
548 Development (FEDER). We would like to acknowledge the AERONET team at NASA/Goddard
549 Space Flight Center in Greenbelt, MD, and Service National d'Observation PHOTONS from
550 University of Lille/CNRS/INSU operating under ACTRIS-FR research infrastructure, for
551 providing high-quality data. Development of lidar data analysis algorithms was supported by
552 Russian Science Foundation (project 16-17-10241).

553

554



555
556 Table 1. Lidar ratios S_{355} , S_{532} for five smoke episodes in December 2015 – January 2016 and
557 corresponding the relative humidity RH. The table provides also the height and temporal interval
558 of observations. The contribution of the smoke particles to the total backscattering $\frac{\beta_{532}^s}{\beta_{532}}$ is derived
559 from depolarization measurements.
560

Date	Height, m	Time, UTC	$\frac{\beta_{532}^s}{\beta_{532}}$	RH, %	S_{355} , sr	S_{532} , sr
15 Dec	2000	04:00-06:00	0.57	42±8	67±7	44±5
15 Dec	1850	19:20-20:30	0.57	25±6	62±6	50±5
23 Dec	2250	05:00-07:00	0.65	65±13	76±8	56±6
24 Dec	3200	19:00-23:00	0.66	75±14	76±8	62±6
20 Jan	4500	01:00-07:00	0.8	85±15	80±8	66±7

561
562



563 **References**

- 564 Amiridis, V., Balis, D. S., Kazadzis, S., Bais, A., Giannakaki, E., Papayannis, A., and Zerefos, C.:
565 Four-year aerosol observations with a Raman lidar at Thessaloniki, Greece, in the framework
566 of European Aerosol Research Lidar Network (EARLINET), *J. Geophys. Res.*, 110, D21203,
567 doi:10.1029/2005JD006190, 2005.
- 568 Alfaro, S. C., Lafon, S., Rajot, J. L., Formenti, P., Gaudichet, A., and Maille, M.: Iron oxides and
569 light absorption by pure desert dust: An experimental study, *J. Geophys. Res.*, 109, D08208,
570 doi:10.1029/2003JD004374, 2004.
- 571 Ansmann, A., Wandinger, U., Riebesell, M., Weitkamp, C. and Michaelis, W., "Independent
572 measurement of extinction and backscatter profiles in cirrus clouds by using a combined Raman
573 elastic-backscatter lidar", *Appl. Opt.* 31, 7113–7131, 1992.
- 574 Ansmann, A., Petzold, A., Kandler, K., Tegen, I., Wendisch, M., Müller, D., Weinzierl, B., Müller,
575 T., Heintzenberg, J.: Saharan Mineral Dust Experiments SAMUM–1 and SAMUM–2: what
576 have we learned?, *Tellus*, 63B, 403–429, 2011.
- 577 Burton, S. P., Vaughan, M. A., Ferrare, R. A. and Hostetler, C. A.: Separating mixtures of aerosol
578 types in airborne High Spectral Resolution Lidar data. *Atmos. Meas. Tech.*, 7, 419–436, 2014.
- 579 Di Biagio, C., Formenti, P., Balkanski, Y., Caponi, L., Cazaunau, M., Pangui, E., Journet, E.,
580 Nowak, S., Caquineau, S., Andreae, M. O., Kandler, K., Saeed, T., Piketh, S., Seibert, D.,
581 Williams, E., and Doussin, J.-F.: Global scale variability of the mineral dust long-wave
582 refractive index: a new dataset of in situ measurements for climate modeling and remote
583 sensing, *Atmos. Chem. Phys.*, 17, 1901–1929, <https://doi.org/10.5194/acp-17-1901-2017>,
584 2017.
- 585 Di Biagio, C., Formenti, P., Balkanski, Y., Caponi, L., Cazaunau, M., Pangui, E., Journet, E.,
586 Nowak, S., Andreae, M. O., Kandler, K., Saeed, T., Piketh, S., Seibert, D., Williams, E., and
587 Doussin, J. – F.: Complex refractive indices and single scattering albedo of global dust aerosols
588 in the shortwave spectrum and relationship to iron content and size, *Atm. Chem. Phys.*, 19,
589 15503–15531, 2019.
- 590 Dubovik, O., Sinyuk, A., Lapyonok, T., Holben, B.N., Mishchenko, M., Yang, P., Eck, T.F.,
591 Volten, H., Munoz, O., Veihelmann, B., van der Zande, W.J., Leon, J.-F., Sorokin, M.,
592 Slutsker, I.: Application of spheroid models to account for aerosol particle nonsphericity in
593 remote sensing of desert dust, *J. Geophys. Res.*, 111, D11208, doi:10.1029/2005JD006619,
594 2006.
- 595 Esselborn, M., Wirth, M., Fix, A., Weinzierl, B., Rasp, K., Tesche, M., and Petzold, A.: Spatial
596 distribution and optical properties of Saharan dust observed by airborne high spectral resolution



- 597 lidar during SAMUM 2006, *Tellus B*, 61, 131–143, doi:10.1111/j.1600-0889.2008.00394.x,
598 2009.
- 599 Freudenthaler, V., Esselborn, M., Wiegner, M., Heese, B., Tesche, M. and co-authors:
600 Depolarization ratio profiling at several wavelengths in pure Saharan dust during SAMUM
601 2006, *Tellus B*, 61B, 165–179, 2009.
- 602 Gasteiger, J., Wiegner, M., Groß, S., Freudenthaler, V., Toledano, C., Tesche, M., and Kandler,
603 K.: Modeling lidar-relevant optical properties of complex mineral dust aerosols, *Tellus B*,
604 63, 725–741, 2011.
- 605 Gelaro, R., McCarty, W., Suarez, M.J., Todling, R., Molod, A., Takacs, L., Randles, C.A.,
606 Darmenov, A., Bosilovich, M.G., Reichle, R., Wargan, K., Coy, L., Cullather, R., Draper,
607 C., Akella, S., Buchard, V., Conaty, A., Da Silva, A.M., Gu, W., Kim, G.K., Koster, R.,
608 Lucchesi, R., Merkova, D., Nielsen, J.E., Partyka, G., Pawson, S., Putman, W., Rienecker,
609 M., Schubert, S.D., Sienkiewicz, M., and Zhao, B.: The Modern-Era Retrospective Analysis
610 for Research and Applications, Version 2 (MERRA-2), *Journal of Climate*, 30, 5419–5454
611 2017.
- 612 Giannakaki, E., van Zyl, P. G., Müller, D., Balis, D., and Komppula, M.: Optical and
613 microphysical characterization of aerosol layers over South Africa by means of multi-
614 wavelength depolarization and Raman lidar measurements, *Atmos. Chem. Phys.*, 16, 8109–
615 8123, 2016.
- 616 Groß, S., Tesche, M., Freudenthaler, V., Toledano, C., Wiegner, M., Ansmann, A., Althausen, D.,
617 and Seefeldner, M.: Characterization of Saharan dust, marine aerosols and mixtures of
618 biomass burning aerosols and dust by means of multi-wavelength depolarization and Raman
619 lidar measurements during SAMUM 2, *Tellus B*, 63, 706724, doi:10.1111/j.1600-
620 0889.2011.00556.x, 2011.
- 621 Haywood, J. M., Pelon, J., Formenti, P., Bharmal, N., Brooks, M., Capes, G., Chazette, P., Chou,
622 C., Christopher, S., Coe, H., Cuesta, J., Derimian, Y., Desboeufs, K., Greed, G., Harrison, M.,
623 Heese, B., Highwood, E. J., Johnson, B., Mallet, M., Marticorena, B., Marsham, J., Milton, S.,
624 Myhre, G., Osborne, S. R., Parker, D. J., Rajot, J. L., Schulz, M., Slingo, A., Tanre, D., and
625 Tulet, P.: Overview of the Dust and Biomass-burning Experiment and African Monsoon
626 Multidisciplinary Analysis Special Observing Period-0, *Journal of Geophysical Research-
627 Atmospheres*, 113, 10.1029/2008jd010077, 2008.
- 628 Hammer, M. S., Martin, R. V., van Donkelaar, A., Buchard, V., Torres, O., Ridley, D. A., and
629 Spurr, R. J. D.: Interpreting the ultraviolet aerosol index observed with the OMI satellite
630 instrument to understand absorption by organic aerosols: implications for atmospheric
631 oxidation and direct radiative effects, *Atmos. Chem. Phys.*, 16, 2507–2523, 2016.



- 632 Hess, M., Koepke, P., and Schult, I.: Optical properties of aerosols and clouds: The software
633 package OPAC, *Bulletin of the American Meteorological Society*, 79, 831–844, 1998.
- 634 Hofer, J., Althausen, D., Abdullaev, S. F., Makhmudov, A. N., Nazarov, B. I., Schettler, G.,
635 Engelmann, R., Baars, H., Fomba, K. W., Müller, K., Heinold, B., Kandler, K., and Ansmann,
636 A.: Long-term profiling of mineral dust and pollution aerosol with multiwavelength
637 polarization Raman lidar at the Central Asian site of Dushanbe, Tajikistan: case studies, *Atmos.*
638 *Chem. Phys.*, 17, 14559–14577, 2017.
- 639 Hofer, J., Ansmann, A., Althausen, D., Engelmann, R., Baars, H., Abdullaev, S.F., and
640 Makhmudov, A.N.: Long-term profiling of aerosol light-extinction, particle mass, cloud
641 condensation nuclei, and ice-nucleating particle concentration over Dushanbe, Tajikistan, in
642 Central Asia, *Atm. Chem. Phys. Disc.* doi.org/10.5194/acp-2019-963.
- 643 Holben, B.N., Eck, T.F., Slutsker, I., Tanre, D., Buis, J.P., Setzer, A., Vermote, E., Reagan, J.A.,
644 Kaufman, Y.J., Nakajima, T., Lavenu, F., Jankowiak, I., Smirnov, A.: AERONET- A federated
645 instrument network and data archive for aerosol characterization. *Remote Sensing of*
646 *Environment* 66, 1-16, 1998.
- 647 IPCC: Climate Change 2013: The Physical Science Basis. Contribution of Working Group I to the
648 Fifth Assessment Report of the Intergovernmental Panel on Climate Change, edited by: Stocker,
649 T. F., Qin, D., Plattner, G.-K., Tignor, M., Allen, S. K., Boschung, J., Nauels, A., Xia, Y., Bex,
650 V., and Midgley, P. M., Cambridge University Press, Cambridge, UK and New York, NY,
651 USA, 1535 pp., <https://doi.org/10.1017/CBO9781107415324>, 2013.
- 652 Kandler, K., Lieke, K., Benker, N., Emmel, C., Küpper, M., Müller-Ebert, D., Ebert, M.,
653 Scheuvs, D., Schladitz, A., Schütz, L., Weinbruch, S.: Electron microscopy of particles
654 collected at Praia, Cape Verde, during the Saharan Mineral Dust Experiment: Particle
655 chemistry, shape, mixing state and complex refractive index. *Tellus* 63B, 475-496, 2011.
- 656 Kirchstetter, T. W., Novakov, T., and Hobbs, P. V.: Evidence that the spectral dependence of light
657 absorption by aerosols is affected by organic carbon, *J. Geophys. Res.-Atmos.*, 109, D21208,
658 <https://doi.org/10.1029/2004JD004999>, 2004.
- 659 Lafon, S., Sokolik, I. N., Rajot, J. L., Caquineau, S., & Gaudichet, A.: Characterization of iron
660 oxides in mineral dust aerosols: Implications for light absorption. *Journal of Geophysical*
661 *Research*, 111(D21), 2006. <https://doi.org/10.1029/2005JD007016>
- 662 Legrand, M., Bertrand, J. J., Desbois, M., Menenger, L., and Fouquart, Y.: The potential of infrared
663 satellite data for the retrieval of Saharan – dust optical depth over Africa, *Journal of Applied*
664 *Meteorology*, 28, 309-319, 1989.



- 665 Legrand, M., Plana-Fattori, A., and N'Doume, C.: Satellite detection of dust using the IR imagery
666 of Meteosat 1. Infrared difference dust index, *Journal of Geophysical Research-Atmospheres*,
667 106, 18251-18274, 2001.
- 668 Mamouri, R. E., Ansmann, A., Nisantzi, A., Kokkalis, P., Schwarz, A., and Hadjimitsis, D.: Low
669 Arabian dust extinction-to-backscatter ratio, *Geophys. Res. Lett.*, 40, 4762–4766, 2013.
- 670 Mattis, I., Ansmann, A., Müller, D., Wandinger, U., and Althausen, D.: Dual-wavelength Raman
671 lidar observations of the extinction-to-backscatter ratio of Saharan dust, *Geophys. Res. Lett.*,
672 29, 1306, doi:10.1029/2002GL014721, 2002.
- 673 Meng, Z., Yang, P., Kattawar, G. W., Bi, L., Liou, K. N., Laszlo, I.: Single-scattering properties
674 of tri-axial ellipsoidal mineral dust aerosols: A database for application to radiative transfer
675 calculations, *J. Aerosol Science* 41, 501–512, 2010.
- 676 Mona, L., Amodeo, A., Pandolfi, M., and Pappalardo, G.: Saharan dust intrusions in the
677 Mediterranean area: three years of Raman lidar measurements, *J. Geophys. Res.*, 111,
678 D16203, doi:10.1029/2005JD006569, 2006.
- 679 Nisantzi, A., Mamouri, R. E., Ansmann, A., Schuster, G. L., and Hadjimitsis, D. G.: Middle East
680 versus Saharan dust extinction-to-backscatter ratios, *Atmos. Chem. Phys.*, 15, 7071–7084,
681 2015.
- 682 Papayannis, A., Amiridis, V., Mona, L., Tsaknakis, G., Balis, D., Bösenberg, J., Chaikovski, A.,
683 De Tomasi, F., Grigorov, I., Mattis, I., Mitev, V., Müller, D., Nickovic, S., Pérez, C.,
684 Pietruczuk, A., Pisani, G., Ravetta, F., Rizi, V., Sicard, M., Trickl, T., Wiegner, M., Gerding,
685 M., Mamouri, R. E., D'Amico, G., and Pappalardo, G.: Systematic lidar observations of
686 Saharan dust over Europe in the frame of EARLINET (2000–2002), *J. Geophys. Res.*, 113,
687 D10204, doi:10.1029/2007JD009028, 2008.
- 688 Papayannis, A., Mamouri, R. E., Amiridis, V., Remoundaki, E., Tsaknakis, G., Kokkalis, P.,
689 Veselovskii, I., Kolgotin A., Nenes, A. and Fountoukis, C.: Optical-microphysical properties of
690 Saharan dust aerosols and composition relationship using a multi-wavelength Raman lidar, in
691 situ sensors and modelling: a case study analysis”, *Atmos. Chem. Phys.* 12, 4011-4032 (2012).
- 692 Perrone, M. R., Barnaba, F., De Tomasi, F., Gobbi, G. P., and Tafuro, A. M.: Imaginary refractive-
693 index effects on desert-aerosol extinction versus backscatter relationships at 351 nm: numerical
694 computations and comparison with Raman lidar measurements, *Appl. Opt.*, 43, 5531 – 5541,
695 2004.
- 696 Preißler, J., Wagner, F., Guerrero-Rascado, J. L., and Silva, A. M.: Two years of free-tropospheric
697 aerosol layers observed over Portugal by lidar, *J. Geophys. Res.-Atmos.*, 118, 3676–3686,
698 doi:10.1002/jgrd.50350, 2013.



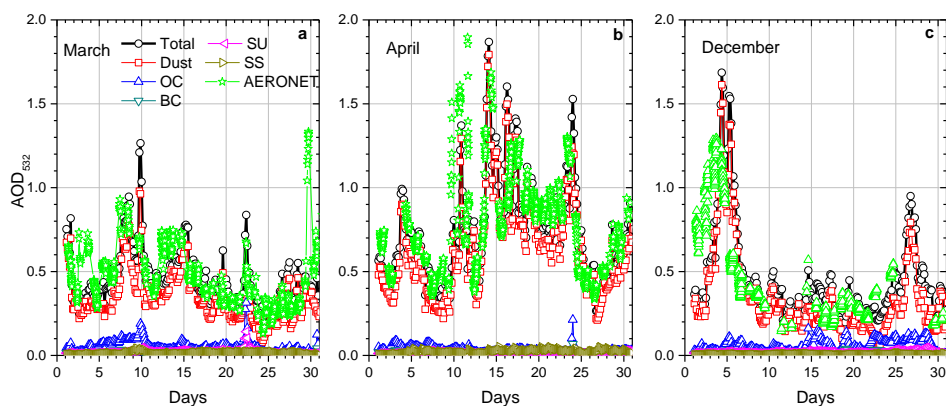
- 699 Randles, C.A., Da Silva, A.M., Buchard, V., Colarco, P.R., Darmenov, A., Govindaraju, R.,
700 Smirnov, A., Holben, B., Ferrare, R., Hair, J., Shinozuka, Y., and Flynn, J.: The MERRA-2
701 Aerosol Reanalysis, 1980 Onward. Part I: System Description and Data Assimilation
702 Evaluation, *J. of Climate*, 30, 6823–6850, 2017.
- 703 Rittmeister, F., Ansmann, A., Engelmann, R., Skupin, A., Baars, H., Kanitz, T., and Kinne, S.:
704 Profiling of Saharan dust from the Caribbean to western Africa – Part 1: Layering structures
705 and optical properties from shipborne polarization/Raman lidar observations, *Atmos. Chem.*
706 *Phys.*, 17, 12963–12983, <https://doi.org/10.5194/acp-17-12963-2017>, 2017.
- 707 Sakai, T., Nagai, T., Nakazato, M., Mano, Y., and Matsumura, T.: Ice clouds and Asian dust
708 studied with lidar measurements of particle extinction-to-backscatter ratio, particle
709 depolarization, and water-vapor mixing ratio over Tsukuba, *Appl. Optics*, 42, 7103–7116,
710 2003.
- 711 Shin, S.-K., Tesche, M., Kim, K., Kezoudi, M., Tatarov, B., Müller, D., and Noh, Y.: On the
712 spectral depolarization and lidar ratio of mineral dust provided in the AERONET version 3
713 inversion product, *Atm. Chem. Phys.*, 18, 12735–12746, 2018.
- 714 Sokolik, I. N., and Toon, O.B.: Incorporation of mineralogical composition into models of the
715 radiative properties of mineral aerosol from UV to IR wavelengths, *J. Geophys. Res.* 104, D8,
716 9423 – 9444, 1999.
- 717 Sun, H., Biedermann, L., and Bond, T. C.: Color of brown carbon: A model for ultraviolet and
718 visible light absorption by organic carbon aerosol, *Geophys. Res. Lett.*, 34, L17813,
719 <https://doi.org/10.1029/2007GL029797>, 2007.
- 720 Tesche, M., Ansmann, A., Müller, D., Althausen, D., Mattis, I., Heese, B., Freudenthaler, V.,
721 Wiegner, M., Eseelborn, M., Pisani, G., and Knippertz, P.: Vertical profiling of Saharan dust
722 with Raman lidars and airborne HSRL in southern Morocco during SAMUM, *Tellus B*, 61,
723 144–164, 2009.
- 724 Tesche, M., Groß, S., Ansmann, A., Müller, D., Althausen, D., Freudenthaler, V., and Esselborn,
725 M.: Profiling of Saharan dust and biomass-burning smoke with multiwavelength polarization
726 Raman lidar at Cape Verde, *Tellus B*, 63, 649–676, doi:10.1111/j.1600-0889.2011.00548.x,
727 2011.
- 728 Torres, O., Tanskanen, A., Veihelmann, B., Ahn, C., Braak, R., Bhartia, P.K., Veefkind, P., and
729 Levelt, P.: Aerosols and surface UV products from Ozone Monitoring Instrument
730 observations: An overview, *J. Geophys. Res.*, 112, D24S47, doi:10.1029/2007JD008809,
731 2007.



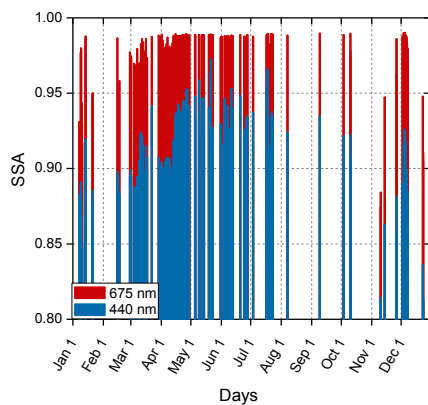
- 732 Veselovskii I., Kolgotin, A., Griaznov, V., Müller, D., Wandinger, U., Whiteman, D.: Inversion
733 with regularization for the retrieval of tropospheric aerosol parameters from multi-wavelength
734 lidar sounding, *Appl.Opt.* 41, 3685-3699, 2002.
- 735 Veselovskii I., O. Dubovik, A. Kolgotin, T. Lapyonok, P. Di Girolamo, D. Summa, D. N.
736 Whiteman, M. Mishchenko, and D. Tanré, 2010: Application Of Randomly Oriented
737 Spheroids For Retrieval Of Dust Particle Parameters From Multiwavelength Lidar
738 Measurements, *J. Geophys. Res.*, **115**, D21203, doi:10.1029/2010JD014139, 2010.
- 739 Veselovskii, I., Whiteman, D. N., Korenskiy, M., Suvorina, A., Perez-Ramirez, D.: Use of
740 rotational Raman measurements in multiwavelength aerosol lidar for evaluation of particle
741 backscattering and extinction, *Atmos. Meas. Tech.*, 8, 4111–4122, 2015.
- 742 Veselovskii, I., Goloub, P., Podvin, T., Bovchaliuk, V., Derimian, Y., Augustin, P., Fourmentin,
743 M., Tanre, D., Korenskiy, M., Whiteman, D., Diallo, A., Ndiaye, T., Kolgotin, A., Dubovik,
744 O.: Study of African dust with multi-wavelength Raman lidar during the “SHADOW”
745 campaign in Senegal, *Atm. Chem. Phys.* 16, 7013–7028, 2016.
- 746 Veselovskii, I., P. Goloub, T. Podvin, et al.: Characterization of smoke/dust episode over West
747 Africa: comparison of MERRA-2 modeling with multiwavelength Mie-Raman lidar
748 observations, *Atm. Meas. Tech.* 11, 949–969, 2018.
- 749 Wagner, R., Ajtai, T., Kandler, K., Lieke, K., Linke, C., Müller, T., Schnaiter, M., and Vragel, M.:
750 Complex refractive indices of Saharan dust samples at visible and near UV wavelengths: a
751 laboratory study, *Atmos. Chem. Phys.*, 12, 2491–2512, 2012.
- 752 Whiteman, D., Melfi, S., Ferrare, R.: Raman lidar system for measurement of water vapor and
753 aerosols in the Earth's atmosphere", *Appl. Opt.* 31, 3068-3082, 1992.
- 754 Xie, C., Nishizawa, T., Sugimoto, N., Matsui, I., and Wang, Z.: Characteristics of aerosol optical
755 properties in pollution and Asian dust episodes over Beijing, China, *Appl. Opt.*, 47, 4945 – 4951,
756 2008.
- 757



758
759



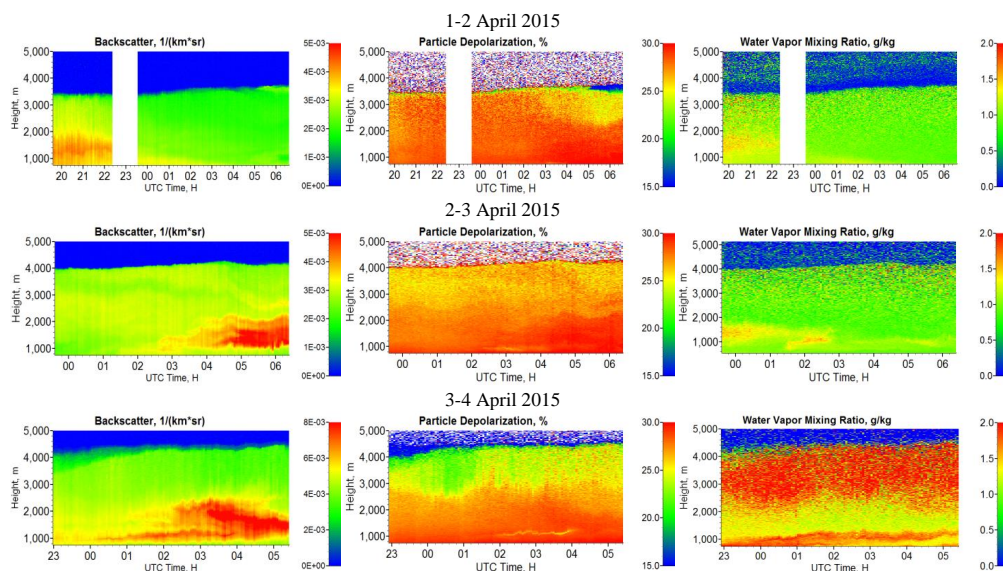
760 Fig.1. The aerosol optical depth (AOD) at 532 nm (open circles) and AODs of the main aerosol
761 components, such as dust, organic carbon (OC), black carbon (BC), sulfates (SU) and sea salt (SS)
762 provided by the MERRA-2 for (a) March, (b) April and (c) December 2015 over Mbour. Open
763 stars show AOD₅₃₂ provided by AERONET.
764
765



766 Fig.2. Aerosol single scattering albedo (SSA) at 675 nm and 440 nm provided by AERONET for
767 Mbour site in 2015.
768
769

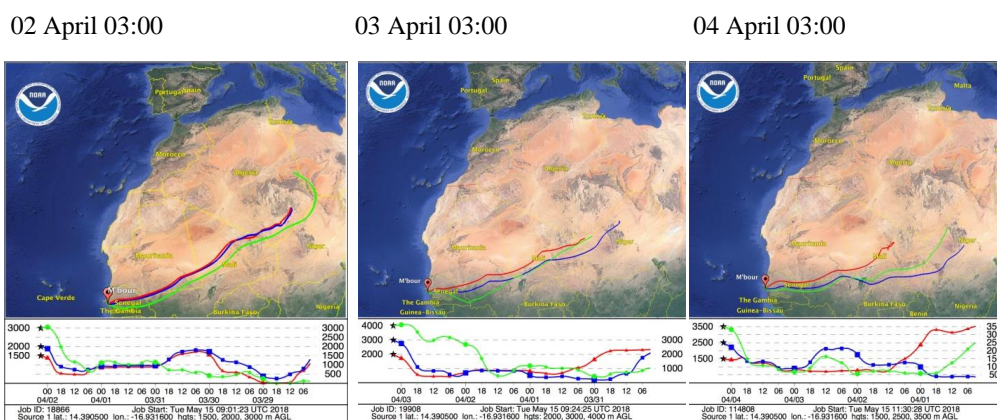


770
 771

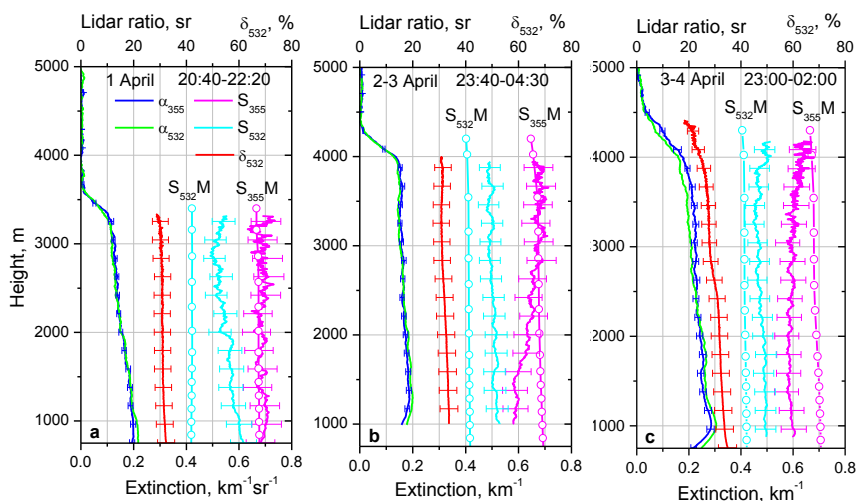


772 Fig.3. Tempo-spatial distributions of aerosol backscattering coefficient β_{532} (left column), particle
 773 depolarization ratio δ_{532} (middle column) and water vapor mixing ratio (right column) for the
 774 nights 1-2 April (upper row), 2-3 April (middle row) and 3-4 April 2015 (bottom row).
 775

776
 777
 778

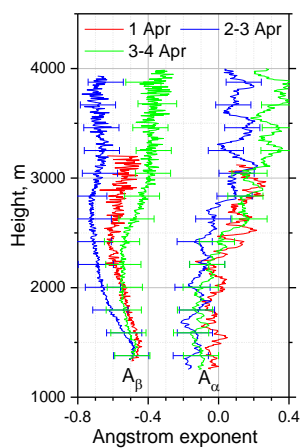


779 Fig.4. Three-day backward trajectories from the NOAA HYSPLIT model for the air mass in
 780 M'bour on 2, 3, 4 April 2015 at 03:00 UTC.
 781



782 Fig.5. Vertical profiles of extinction coefficients (α_{355} , α_{532}) and lidar ratios (S_{355} , S_{532}) at 355 nm
 783 and 532 nm together with particle depolarization ratio δ_{532} measured on 1 April (20:40-22:20
 784 UTC), 2-3 April (23:40-04:30 UTC) and 3-4 April 2015 (23:00-02:00 UTC). Symbols show the
 785 lidar ratios of dust provided by MERRA-2 model (S_{355M} , S_{532M}).

786



787

788 Fig.6. Vertical profiles of the extinction and backscattering Ångström exponents (A_α and A_β) at
 789 355 – 532 nm for three temporal intervals from Fig.5.

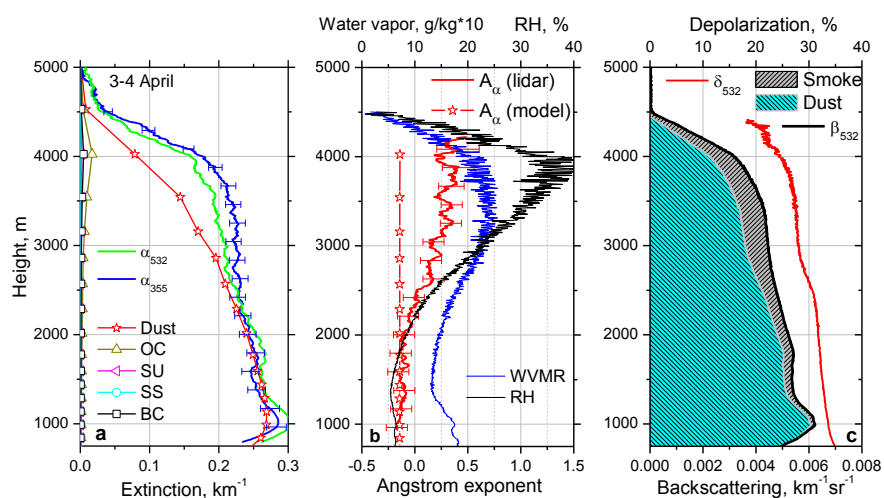
790

791



792

793



794 Fig.7. Vertical profiles of (a) extinction coefficients at 355 nm and 532 nm (α_{355} , α_{532}) measured
795 by lidar (lines) and modeled by MERRA-2 (line+symbol) for five aerosol components at 532 nm;
796 (b) extinction Ångström exponents at 355-532 nm obtained from lidar observations and modeled
797 by MERRA-2 for pure dust (stars) together with water vapor mixing ratio (WVMR) and the
798 relative humidity; (c) contribution of dust and smoke particles to β_{532} together with particle
799 depolarization ratio δ_{532} . Values of WVMR are multiplied by factor 10. Lidar measurements were
800 performed on 3-4 April 2015 for period 23:00 – 02:00 UTC. Modeling results are given for 4 April
801 00:00 UTC.

802

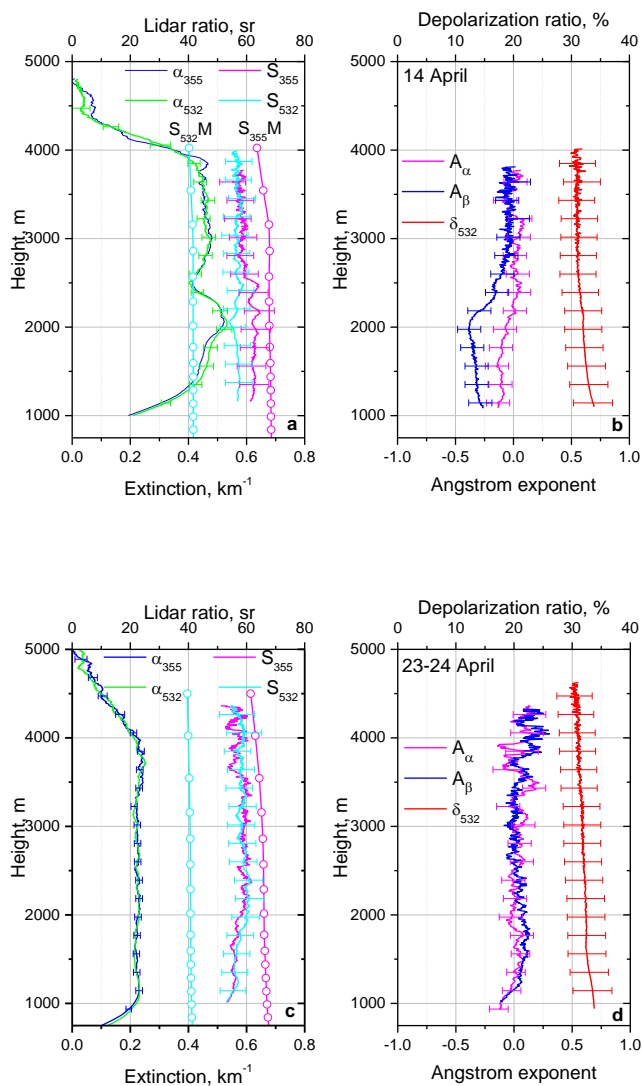
803



804

805

806

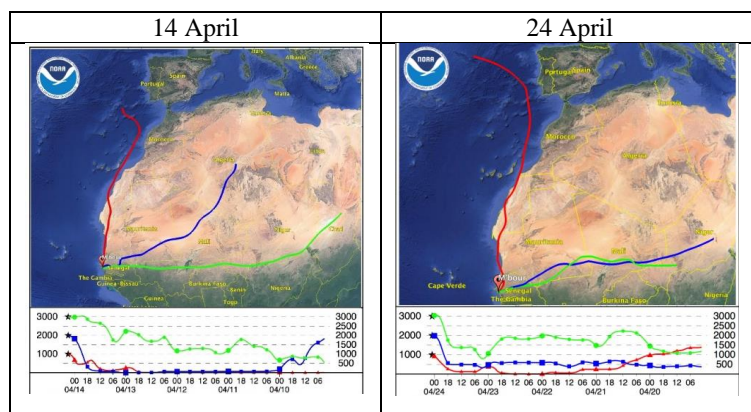


807 Fig.8. (a, c) Vertical profiles of extinction coefficients (α_{355} , α_{532}) and lidar ratios (S_{355} , S_{532}) at
808 355 nm and 532 nm; together with (b, d) particle depolarization ratio δ_{532} , and extinction and
809 backscattering Ångström exponents (A_α , A_β) measured on (a, b) 14 April 2015 (00:00 – 05:00
810 UTC) and (c, d) the night 23-24 April (23:00-06:00 UTC). Open symbols on plots (a, c) show the
811 lidar ratios S_{355M} and S_{532M} provided by MERRA-2 model on 14 and 14 April at 00:00 UTC.
812
813
814



815

816

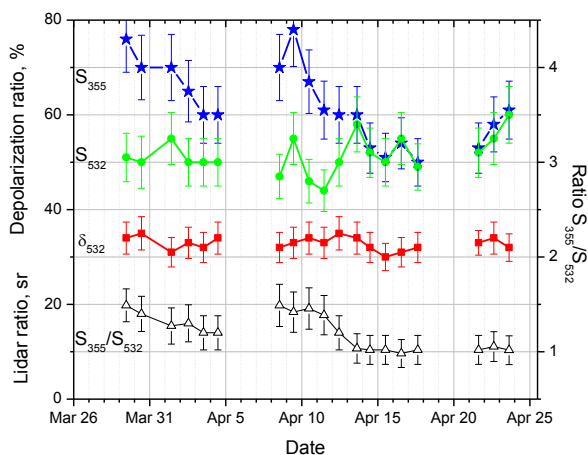


817

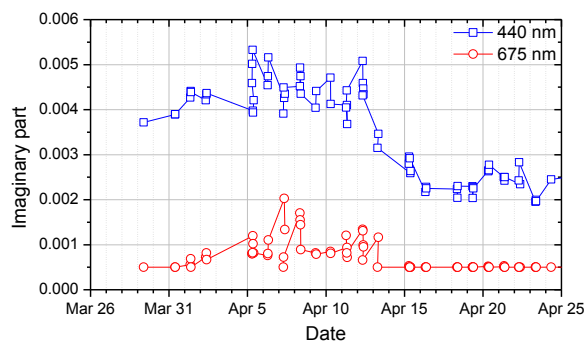
818 Fig.9. Four-days backward trajectories from the NOAA HYSPLIT model for 14 April (03:00
819 UTC) and 24 April (00:00 UTC) 2015.

820

821



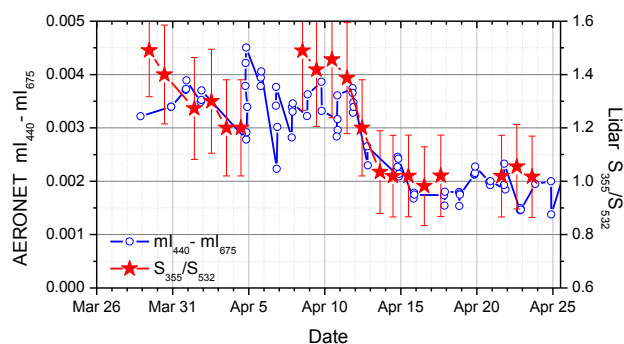
822
823 Fig.10. Lidar ratios S_{355} , S_{532} and the particle depolarization ratio δ_{532} for dust episodes in March
824 - April 2015. Open triangles show the ratio S_{355}/S_{532} .



825
826 Fig.11. Imaginary part of the refractive index at 440 nm and 675 nm provided by AERONET in
827 March – April 2015

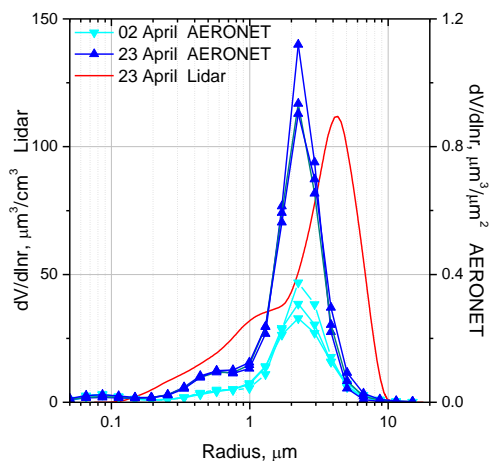


828
829



830
831 Fig. 12. Difference $m_{440} - m_{675}$ from Fig. 11 together with lidar measured values S_{355}/S_{532} from
832 Fig. 10 for days in April 2015.

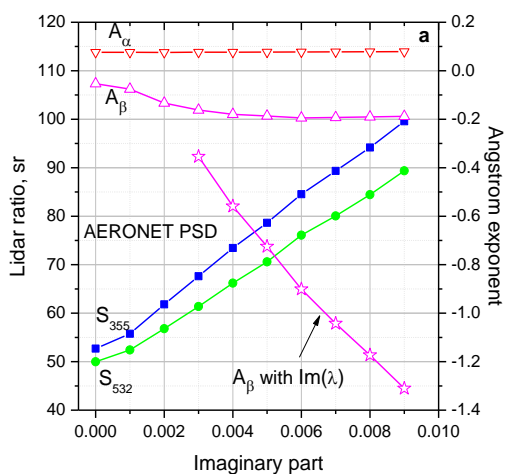
833
834
835
836



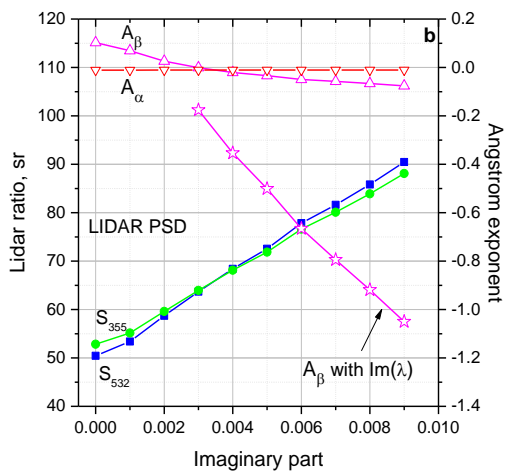
837
838 Fig. 13. The particle size distributions provided by AERONET on 2 and 23 April 2015 (three PSDs
839 for each day). Red line shows the PSD derived from $3\beta+2\alpha$ lidar measurements on 23-24 April.
840
841



842
 843

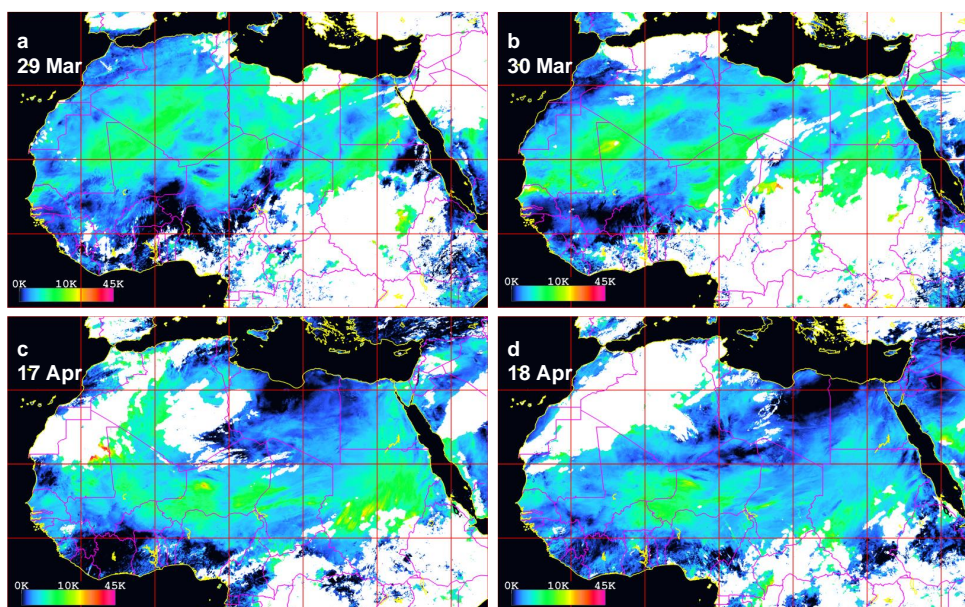


844



845
 846
 847
 848
 849
 850
 851
 852

Fig. 14. Lidar ratios S_{355} , S_{532} together with the extinction and backscattering Ångström exponents A_α and A_β calculated for (a) AERONET PSD on 23 April from Fig.13 and (b) lidar derived PSD from Fig.13 as a function of the imaginary part. Open stars show A_β for spectrally dependent imaginary part $\text{Im}(\lambda)$, assuming that $\text{Im}_{532}=0.002$ is fixed and only Im_{355} is free vary. Computations are performed for the assembly of randomly oriented spheroids with the real part $\text{Re}=1.55$.

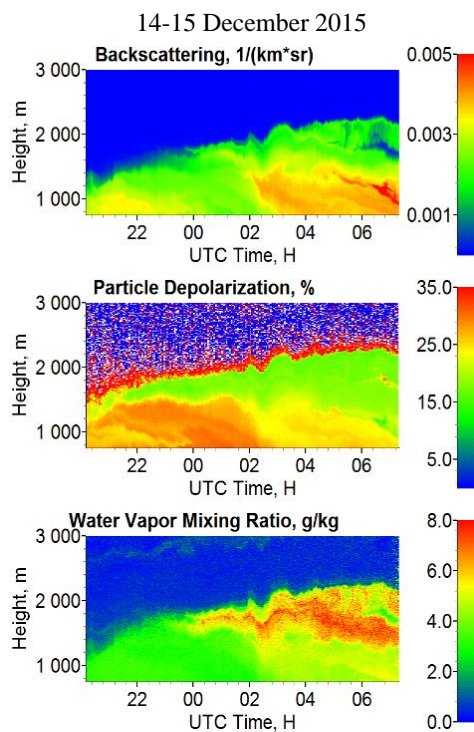


853
854
855
856
857
858
859
860
861
862

Fig.15. Infrared Difference Dust Index (IDDI) derived from MSG geostationary satellite at noon time. Panels (a), (b) show IDDI elevated values, representing airborne dust emission and transport, over central and northern Sahara on 29, 30 March 2015. The dust transport regime is visibly changed a few days later (17, 18 April 2015, panels (c), (d)); the elevated IDDI values are shifted to the south. The areas in white are cloud screened pixels; the IDDI is derived only over land due to the algorithm physical principle.



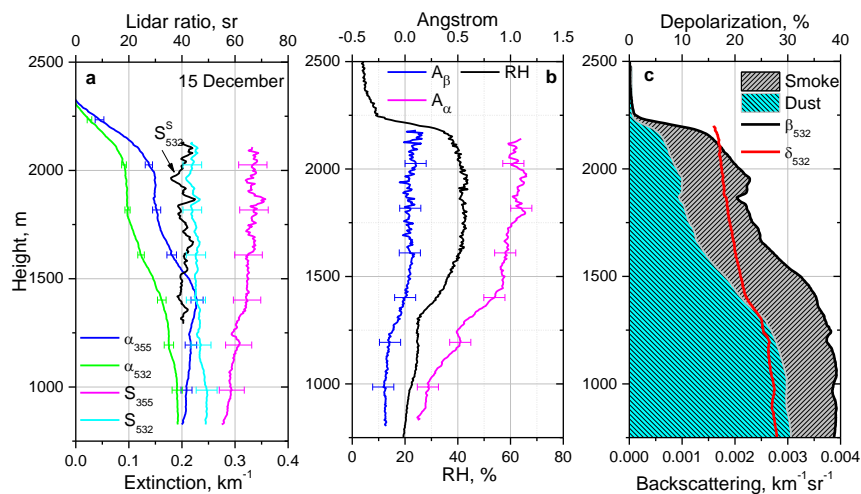
863
864



865 Fig.16. Tempo-spatial distributions of aerosol backscattering coefficient β_{532} ,
866 particle depolarization ratio δ_{532} and water vapor mixing ratio during smoke episode on the night 14-15
867 December 2015.
868
869



870

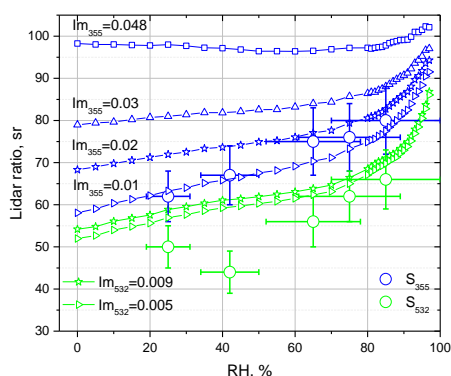


871 Fig.17. Vertical profiles of (a) extinction coefficients (α_{355} , α_{532}) and lidar ratios (S_{355} , S_{532}); (b)
872 extinction, backscattering Ångström exponents (A_α , A_β) at 355 – 532 nm and relative humidity
873 RH; (c) contribution of dust and smoke to β_{532} together with particle depolarization ratio δ_{532} on
874 15 December (04:00 – 06:00 UTC). Black line in plot (a) shows the lidar ratio of smoke S_{532}^s
875 calculated from Eq.5.

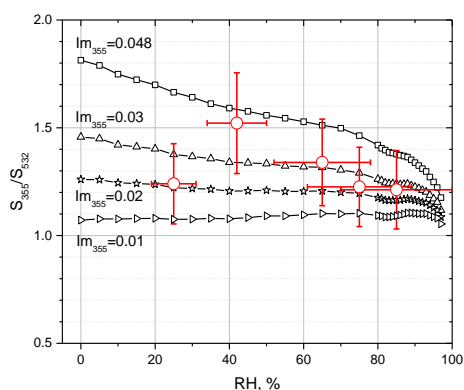
876
877
878



879
880



881
882 Fig. 18. Modeled lidar ratios of organic carbon at 355 nm and 532 nm (line + symbol) as a function
883 of the relative humidity for the particle parameters used in the MERRA-2 model. At 355 nm results
884 are given for four values of the imaginary part of dry particles: $Im_{355} = 0.048, 0.03, 0.02, 0.01$. At
885 532 nm two values $Im_{532} = 0.009$ and 0.005 are considered. The scattered symbols (circles) show
886 the lidar ratios (S_{355}, S_{532}) observed during five smoke episodes from Table 1.
887



888
889 Fig. 19. The ratio S_{355}/S_{532} for organic carbon as a function of the relative humidity calculated from
890 modeling results in Fig. 18 for $Im_{532} = 0.009$ and $Im_{355} = 0.048, 0.03, 0.02, 0.01$. The scattered
891 symbols (circles) show the observed S_{355}/S_{532} values.
892
893